



Spatial variations of rock damage production by earthquakes in southern California



Yehuda Ben-Zion ^{a,*}, Ilya Zaliapin ^b

^a University of Southern California, Department of Earth Sciences, Los Angeles, CA 90089-0740, United States

^b University of Nevada, Reno, Department of Mathematics and Statistics, Reno, NV 89557, United States

ARTICLE INFO

Article history:

Received 18 August 2018

Received in revised form 27 January 2019

Accepted 3 February 2019

Available online xxxx

Editor: M. Ishii

Keywords:

earthquakes

rock damage

fault zones

background seismicity

southern California

ABSTRACT

We perform a comparative spatial analysis of inter-seismic earthquake production of rupture area and volume in southern California using observed seismicity and basic scaling relations from earthquake phenomenology and fracture mechanics. The analysis employs background events from a declustered catalog in the magnitude range $2 \leq M < 4$ to get temporally stable results representing activity during a typical inter-seismic period on all faults. Regions of high relative inter-seismic damage production include the San Jacinto fault, South Central Transverse Ranges especially near major fault junctions (Cajon Pass and San Gorgonio Pass), Eastern CA Shear Zone (ECSZ) and the Imperial Valley – Brawley seismic zone area. These regions are correlated with low velocity zones in detailed tomography studies. A quasi-linear zone with ongoing damage production extends between the Imperial fault and ECSZ and may indicate a possible future location of the main plate boundary in the area. The regions around the 1992 M6.1 Joshua Tree, M7.3 Landers and M6.3 Big Bear earthquakes have background seismic activity before 1990. This may represent a regional weakening process by damage production in future rupture zones. The depth of background seismicity and damage production decreases steadily from SW of the coastline to NE of the San Andreas fault, and also to the SE near the US–Mexico border. The seismicity and rock damage become more pronounced and continuous along-strike of main faults with increasing depth.

© 2019 Elsevier B.V. All rights reserved.

1. Introduction

Earthquake ruptures produce rock damage in their source volumes associated with increased crack density and related changes of elastic moduli, mass density, seismic velocities, attenuation, anisotropy, permeability, conductivity and other rock properties (e.g., Lockner et al., 1977; Dresen and Gueguen, 2004; Mavko et al., 2009). The evolution of rock damage reflects key processes leading to large brittle instabilities (e.g., Peng and Johnson, 1972; Hamiel et al., 2004; Renard et al., 2018). On longer timescales, the cumulative effects of rock damage over geological time can modify significantly the properties and dynamics of fault zones and the crust (e.g., Lyakhovsky et al., 2001; Ben-Zion, 2008; Sibson, 2011; Jamtveit et al., 2018). Estimating the production of rock damage by earthquakes can provide useful information for various studies in seismically active regions. For example, seismic imaging studies derive P and S velocity models, attenuation coefficients and related quantities in the crust (e.g., Lin et al., 2007;

Eberhart-Phillips et al., 2014; Fang et al., 2016). However, the derived properties are affected strongly by several attributes including rock composition, crack density and fluid content (which depend largely on the crack density). Interpreting the derived results in terms of a given factor (e.g., rock type) requires making assumptions on the others. Other examples of research topics that can benefit from estimated seismic production of rock damage include exploration of resources and induced seismicity (e.g., Schoenball and Ellsworth, 2017; Atkinson et al., 2016), crustal hydrology (e.g., Sibson et al., 1975; Hickman et al., 1995) and erosion and landslide patterns (e.g., Wechsler et al., 2009; Scheingross et al., 2013; Marc et al., 2015).

In the present paper we attempt to estimate the inter-seismic production of fracture area and rupture volume by earthquakes in southern California using observed seismicity and basic scaling relations from earthquake phenomenology and fracture mechanics. The analysis employs the southern California earthquake catalog of Hauksson et al. (2012; extended to later years) for the period 1981–2017. The study aims to estimate the relative seismic production of rock damage in different parts of the broad plate-boundary region in southern California. Since large earthquakes

* Corresponding author.

E-mail addresses: benzion@usc.edu (Y. Ben-Zion), zal@unr.edu (I. Zaliapin).

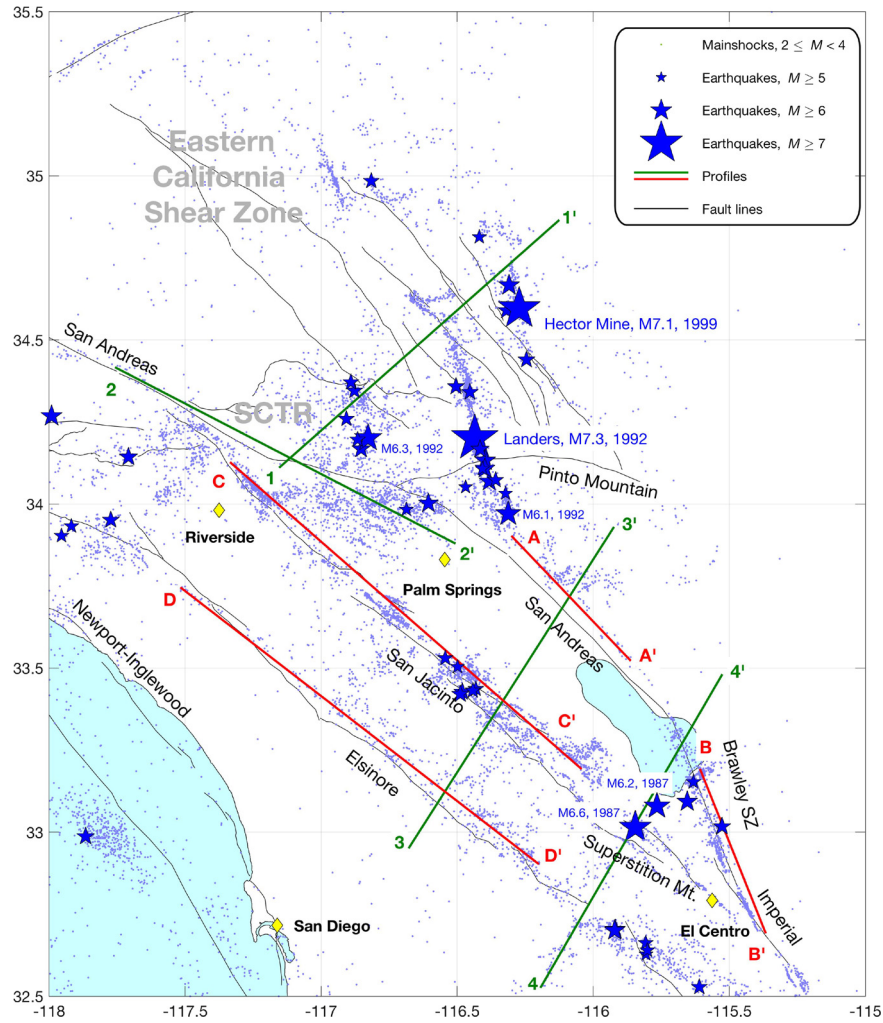


Fig. 1. The study area in southern California. Dots show epicenters of the examined background earthquakes with magnitude $2 \leq M < 4$. Earthquakes with $M > 5$ (not used in the damage estimation) are shown by blue stars with size proportional to the magnitude. Black lines show major faults. Green and red lines show profiles used in Figs. 3 and 4. Several towns are indicated by yellow symbol and name. SCTR stands for South Central Transverse Ranges. (For interpretation of the colors in the figure(s), the reader is referred to the web version of this article.)

are rare and not properly represented in the used (and any other) instrumental catalog, and seismicity is strongly non-stationary in time with large variations after large earthquakes, we use only earthquakes with magnitude $2 \leq M < 4$ taken from a declustered version of the catalog (Fig. 1). This data set gives an approximate uniform representation of the long-term average inter-seismic seismicity in all parts the study area. The derived estimates can help separating rock damage and composition in models of seismic velocities and attenuation coefficients for the region (e.g., Hauksson and Shearer, 2006; Allam et al., 2014; Share et al., 2019). The results can also highlight seismic zones that are active persistently beyond fluctuations associated with the large events.

The remainder of the paper is organized as follows. In the next section we describe the theoretical relations used to estimate the production of fracture area and volume generated by observed seismicity. Section 3 implements the methodology and provides estimates of rock damage production in southern California. The results indicate the existence of a quasi-linear zone with ongoing damage production between the Imperial fault near the US–Mexico border and the Eastern California Shear Zone in the Mojave Desert. The regions around the 1992 Joshua Tree, Landers and Big Bear earthquakes are active before 1990 and outline the ruptures of the future events. The seismicity and damage zone become more pronounced and continuous along-strike with increasing depth. The implications of these and other results to properties and dynamics

of the plate-boundary region in southern California are discussed in the final section 4.

2. Methodology

Combining basic empirical relations of earthquakes and theoretical results from fracture mechanics can be used to estimate the fracture area and rupture volume associated with a population of earthquakes. The theoretical formulations are provided in Sects. 2.1, 2.2 following generally Jamtveit et al. (2018) with a few additional details. Section 2.3 discusses a practical implementation of the theoretical results using observed earthquake catalog.

2.1. Fracture area

Assume that the total number $N(M)$ of earthquakes with magnitude equal to or above M in the examined spatio-temporal domain is given by the Gutenberg–Richter exponential relation

$$\log_{10} N(M) = a' - bM = a' - bM_0 - b(M - M_0), \quad M \geq M_0, \quad (1a)$$

where a' and b are empirical constants, and M_0 is the minimal examined magnitude (assumed here to be above the magnitude of completeness). The constant b quantifies the relative numbers

of events in different magnitude ranges. The quantity $10^{a'}$ is the projected total number of events above magnitude zero, which is extrapolated from the observed total number $10^{a'-bM_0}$ of events with magnitude $M \geq M_0$ in the catalog. The projected number of events below a given magnitude M (with $M \geq M_0$) is given by $N(M_0) - N(M)$, and the corresponding rate $n(M) = d/dM[N(M_0) - N(M)]$ of events in the magnitude bin $[M, M + dM]$ is

$$\log_{10} n(M) = a - bM, \quad a = a' + \log_{10}[b \ln(10)], \quad M \geq M_0. \quad (1b)$$

The total fracture area generated by a population of earthquakes in the magnitude range $M_1 \leq M \leq M_2$ can be calculated by the integral

$$A_T = \int_{M_1}^{M_2} A(M) \cdot n(M) dM, \quad (2)$$

where $A(M)$ is the fracture area of an earthquake with magnitude M . To get representative comparative results for an interseismic period we use only earthquakes with $2 \leq M < 4$ from a declustered catalog. To estimate $A(M)$, we assume that each earthquake can be approximated as a circular crack with radius r sustaining a uniform strain drop $\Delta\varepsilon$ in a Poissonian solid. This is statistically realistic for the used events. The scalar seismic potency (moment/rigidity) of each such event is given by (Eshelby, 1957; Ben-Zion, 2008)

$$P_0 = (16/7)\Delta\varepsilon r^3. \quad (3)$$

The seismic potency and magnitude of earthquakes spanning a relatively small range of magnitudes (e.g., ≤ 3) are related empirically by a relation of the type (e.g., Hanks and Kanamori, 1979; Ben-Zion, 2008),

$$\log_{10}(P_0) = kM + e. \quad (4)$$

Analysis of over 11,000 earthquakes in the San Jacinto fault zone region indicates that $k = 1.13$ and $e = -4.06$ for $2 \leq M < 4$ with potency units in $\text{km}^2 \times \text{cm}$ (Ross et al., 2016). Similar constants characterize earthquakes with $2 \leq M < 4$ in other data sets (e.g., Ben-Zion and Zhu, 2002; Edwards et al., 2010). Combining (3) and (4), the radius of an earthquake with magnitude M in unit of km is

$$r = \left[\frac{10^{-5}}{(16/7)\Delta\varepsilon} \right]^{1/3} \cdot 10^{1/3 \cdot (k \cdot M + e)}, \quad (5a)$$

where the 10^{-5} factor stems from a unit conversion of P_0 from $\text{km}^2 \times \text{cm}$ to km^3 . Using (5a) for r and assuming again a circular crack,

$$A(M) = \pi \cdot \left[\frac{10^{-5}}{(16/7)\Delta\varepsilon} \right]^{2/3} \cdot 10^{2 \cdot (k \cdot M + e)/3}. \quad (5b)$$

With this, the integral in (2) is written as

$$A(M_1 \leq M \leq M_2) = \pi \cdot \left[\frac{10^{-5}}{(16/7)\Delta\varepsilon} \right]^{2/3} \cdot 10^a \cdot \int_{M_1}^{M_2} 10^{(2k/3 - b) \cdot M} \cdot 10^{2e/3} dM. \quad (6)$$

Carrying out the remaining integral gives

$$A(M_1 \leq M \leq M_2) = c_1 \cdot 10^{2e/3} [e^{\alpha M_2} - e^{\alpha M_1}], \quad (7)$$

with $c_1 = [\pi \frac{1}{\alpha} \frac{10^{-5}}{16\Delta\varepsilon}]^{2/3}$ and $\alpha = [(2k/3) - b]\ln(10)$. For a typical b -value of 1, α is negative so the cumulative production of fracture area is dominated by the smallest earthquakes included in the analysis.

2.2. Rupture volume

The total rupture volume generated by earthquakes in the magnitude range $M_1 \leq M \leq M_2$ can be calculated similarly using

$$V_T = \int_{M_1}^{M_2} A(M) w(M) \cdot n(M) dM, \quad (8)$$

where $w(M)$ is the width (thickness) of the rupture zone generated by an earthquake with magnitude M . From fracture mechanics and numerical simulation results, the width of an off-fault yielding (rupture) zone scales linearly with the rupture radius

$$w(M) = \gamma \cdot r(M), \quad (9)$$

with a constant γ that is proportional to the dynamic stress intensity factor and the ratio of stress drop over strength drop (Ben-Zion and Ampuero, 2009). Hence, the damage volume generated by an individual earthquake of magnitude M is

$$V(M) = \gamma r(M) A(M) = \gamma \pi \cdot \left[\frac{10^{-5}}{(16/7)\Delta\varepsilon} \right] \cdot 10^{k \cdot M + e}. \quad (10)$$

Using this and expressions (2) and (5a), the integral in (8) is

$$V_T(M_1 \leq M \leq M_2) = \pi \gamma \cdot \left[\frac{10^{-5}}{(16/7)\Delta\varepsilon} \right] \cdot 10^{a+e} \cdot \int_{M_1}^{M_2} 10^{(k-b) \cdot M} dM. \quad (11)$$

Integrating (11) gives

$$V_T(M_1 \leq M \leq M_2) = c_2 \cdot [e^{\beta M_2} - e^{\beta M_1}], \quad (12)$$

with $c_2 = \pi \frac{\gamma}{\beta} \frac{7 \cdot 10^{-5}}{16\Delta\varepsilon} 10^{a+e}$ and $\beta = (k - b)\ln(10)$. Since β is positive for a typical b -value of 1, the cumulative production of fracture volume is dominated by the largest earthquakes included in the analysis.

2.3. Implementation using an observed earthquake catalog

We follow the approach of the previous sections to estimate the relative production of fracture area and rupture volume in different parts of southern California by earthquakes associated with ongoing background activity. Absolute estimates of rock damage values are not essential for our goals, and are also not attainable given the short duration of the earthquake catalog and existence of rock healing. To obtain relative damage values, the integrals (6) and (11) are estimated by directly summing the damage area $A(M)$ of Eq. (5b) and damage volume $V(M)$ of Eq. (10) for the analyzed background events in volumetric elements with dimensions that are described below. The resulting values are divided by the time duration of the catalog to obtain average values per year.

We use the catalog of Hauksson et al. (2012) extended to cover the time interval 1981–2017. The analysis is done for the area between $118\text{--}115^\circ\text{W}$ and $32.5\text{--}35.5^\circ\text{N}$ (Fig. 1). As mentioned, we analyze only background events within the magnitude range $2 \leq M < 4$. This reflects our goal to obtain results that are representative for a typical inter-seismic period of all faults in the study area, and to minimize effects associated with moderate and large events that happened to occur within the examined time interval on some faults. The background events are obtained by decomposing the catalog into earthquake clusters using the nearest-neighbor

proximity approach of Zaliapin and Ben-Zion (2013, 2016), and retaining for analysis only mainshocks (the largest events) of the clusters with magnitude in the range $2 \leq M < 4$. Fig. 1 displays the background events used in the study (small dots); for reference we also show all earthquakes with $M \geq 5$ in the study area (blue stars). A visual examination of the earthquakes, and the formal analysis below, show a relatively close match between the location of the $M \geq 5$ events and the bulk of the background seismicity.

The constant γ of Eq. (9) is in the range 0.01–0.001 for typical rupture velocity of 0.9 the Rayleigh wave speed and stress drop that is 10% of the strength drop. In the applications done here we use $\gamma = 1/500$. We also use $\Delta\varepsilon = 10^{-4}$ and empirical constants $k = 1.13$ and $e = -4.06$. The units of the estimated earthquake rupture area are km^2 per yr, and the units of the corresponding estimated rupture volumes are km^3 per yr.

To make the calculations we use a 300×300 rectangular grid with average grid spacing of 10 km at the surface of the examined region between $118\text{--}115^\circ\text{W}$ and $32.5\text{--}35.5^\circ\text{N}$. To every grid point x we assign the cumulative damage volume of all background events with magnitude $2 \leq M < 4$ whose surface projection falls within a circle with radius 5 km centered at x . The cumulative damage values are divided by the time interval duration of 37 yr, to get damage values in units of km^3 per yr. Finally, we smooth the resulting surface map by a symmetric Gaussian filter with a standard deviation of $\sigma = 0.15^\circ$ corresponding approximately to 16 km.

3. Results

Fig. 2a displays a map view of the estimated yearly average of damage volume production for the period 1981–2017. To examine the temporal stability of the estimated damage production with respect to episodic occurrence of large events, we compare (Fig. 2b) the damage volume production before and after 1990 by calculating the proportional change of damage

$$\Delta\text{volume} = (V_{\text{after}} - V_{\text{before}}) / \max(V_{\text{after}}, V_{\text{before}}), \quad (13)$$

where V_{after} , V_{before} are the values of damage volume production rate after and before 1990, respectively. The year 1990 is chosen as a dividing time since the largest event that occurred in the study area and period is the 1992 M7.3 Landers earthquake. By definition $-1 \leq \Delta\text{volume} \leq 1$ and negative/positive values correspond to decrease/increase of damage volume production after 1990. The map views of the average yearly damage production before and after 1990 are shown in Figs. 2c and 2d.

As shown in Fig. 2a, the ongoing background damage production in southern CA is concentrated in several regions including San Jacinto Fault Zone (SJFZ), Brawley Seismic Zone (BSZ), South Central Transverse Ranges (SCTR), Eastern California Shear Zone (ECSZ), and to a lesser extent also Elsinore fault. The rock damage is not distributed uniformly along the seismogenic structures, but is rather concentrated in several permanently active patches (red blobs) associated with significant geometrical complexities. The results highlight the existence of several dominant active damage zones in the southern California plate boundary region. We note that the Imperial fault, BSZ, southern San Andreas Fault and ECSZ form a quasi-linear zone with ongoing damage production. We also note that most moderate-large earthquakes (blue stars in Fig. 2) occur within the main damage zones associated with the low magnitude background events used in the analysis. However, there are some M5 events outside these zones and there are also very active damage areas with no moderate-large events in the last 30 years. This may reflect the fact that some M5 events represent transient signatures of large seismic cycles, while the background events used in this work represent typical interseismic activity.

The rock damage production before and after 1990 is concentrated generally in the same zones (Figs. 2b–d). There are some fluctuations that reflect the relative shortness of the available catalogs, and can be described as a slow migration of the active patches along the seismically active structures within kilometers range, along with some changes in the damage intensity. There also exist large-scale changes (appearance or disappearance) of the active damage production zones. Most damage zones do not show large temporal fluctuations (gray color in Fig. 2b). Significantly, the regions around the 1992 M6.1 Joshua Tree, M7.3 Landers and M6.3 Big Bear earthquakes are active before 1990 and outline the ruptures of the future events (Fig. 2c). The occurrences of these events and the 1999 Hector Mine earthquake are followed by increased damage production in the ECSZ and SCTR, and there is increase damage in the Brawley seismic zone after 1990 that may be associated with onset of geothermal exploration in Salton Sea. Some isolated patches in various places (blue in Fig. 2b) show a decrease of damage production after 1990. Given the relative shortness of the examined catalog and overall complexity of the earthquake process, we find that the damage production by background events is rather stable in space and time across the examined region.

Corresponding maps of fracture area were computed using the same approach and parameters used to obtain to the damage volume results presented in Fig. 2. The two sets of maps are almost indistinguishable up to some scaling dimensional constants, so the calculated fracture area maps are not shown. This similarity is consistent with expressions (7) and (12) for the cumulative damage area and volume. Each of these expressions can be represented as a product of the total number of events in the examined catalog (proportional to 10^a) and a constant that depends on the parameters b , k , e , γ , $\Delta\varepsilon$ (but not on a). In other words, the total damage volume and total damage area are expected to be proportional to each other, with proportionality coefficient K depending on b , k , e , γ , and $\Delta\varepsilon$. Accordingly, if analysis is focused on relative variations of damage values (as is the case in this study), it is sufficient to present only either damage volume or area. The similarity of the estimated total damage volume and area confirms that the analysis is not significantly affected by artifacts of a small sample (e.g., non-stationary patterns of the largest events) and does represent fairly well inter-seismic activity. The expressions provided in Sect. 2 for the total rupture area and volume may be useful for different applications that have a primary interest in estimating either quantity. We note that the numerical ratio K of the estimated total rupture area and volume increases when the lower magnitude boundary extends to smaller events, and decreases when the upper boundary extends to larger events.

Figs. 3 and 4 illustrate the damage volume production across the profiles marked in Fig. 1. Each profile plot is calculated using a rectangle with horizontal side coinciding with the profile on Fig. 1 and vertical extent of 20 km. Each rectangle is spanned by a grid with 300 horizontal and 100 vertical points. To each grid point y , we assign the value of total damage volume within a 3D cylinder that extends 5 km to both sides of the rectangle and whose intersection with the rectangle is a circle of radius 5 km centered at y . As before, we only use background events with magnitudes $2 \leq M < 4$ and the obtained values are divided by the time interval duration of 37 yr. The resulting map is smoothed using an asymmetric Gaussian filter, with vertical standard deviation fixed at $\sigma_v = 3$ km and horizontal standard deviation σ_h that increases with the profile length. For profiles A and B with length of 60 km, we use $\sigma_h = 3$ km; for profiles 1–4 with length of 130 km, $\sigma_h = 6.5$ km; for profiles C and D with length 160 km, $\sigma_h = 8$ km. The results along profiles 1–1', 3–3' and 4–4' (Fig. 3) show significant concentrations of background damage across large faults and rupture zones of the 1992 Landers and 1999 Hector Mine earth-

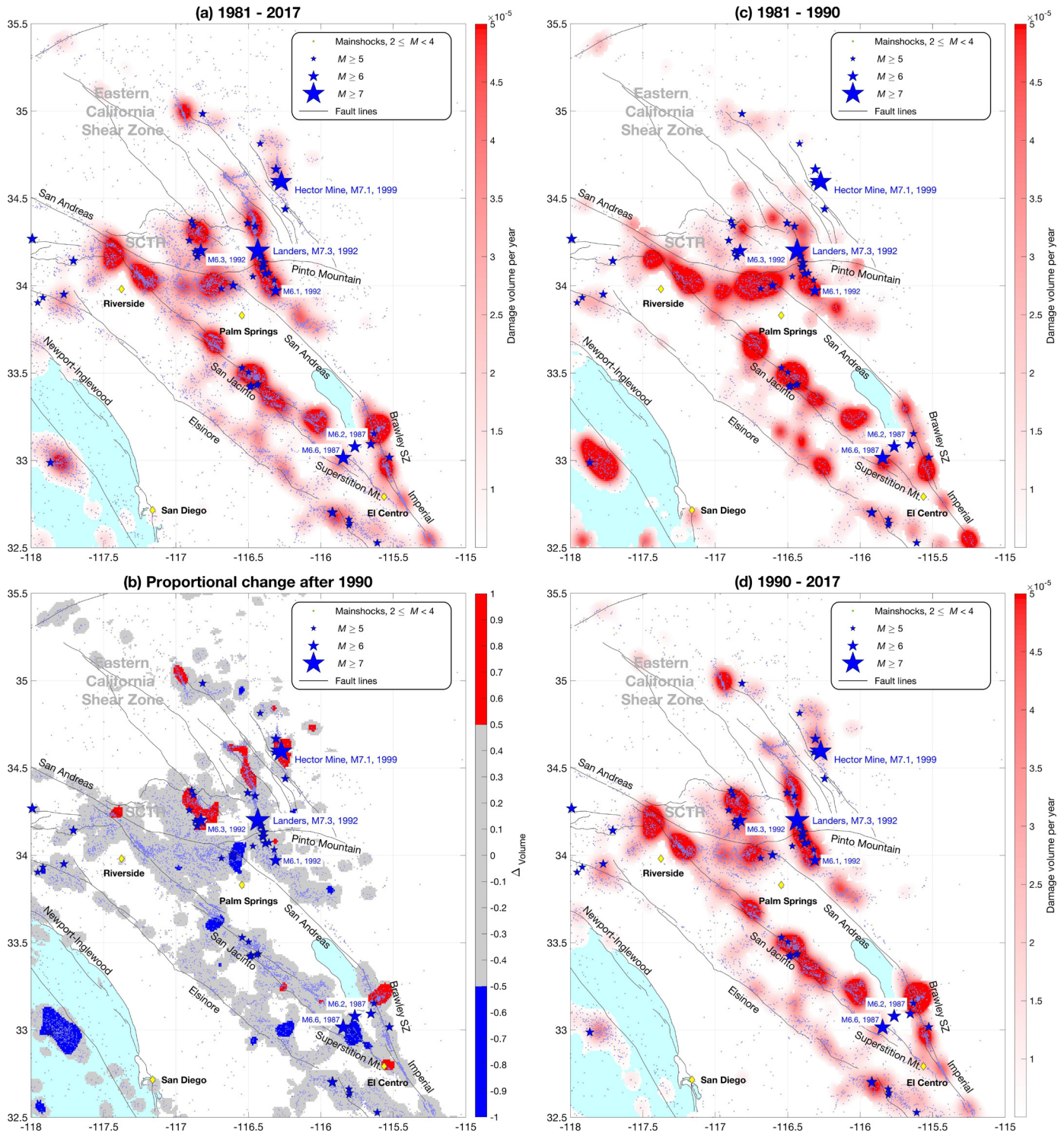


Fig. 2. Estimated damage volume V in $\text{km}^3 \text{yr}^{-1}$ (color code) projected at the earth surface. The damage is estimated using background events with magnitude $2 \leq M < 4$ shown by dots. The other notations are as in Fig. 1. (a) Total damage volume estimated for 1981–2017. (b) Proportional change Δ_{volume} of the damage production after 1990 defined by Eq. (13). Values $\Delta_{\text{volume}} > 0.5$ (damage increase) are shown in red, $\Delta_{\text{volume}} < -0.5$ (damage decrease) are shown in blue, and all other values are gray. (c) Damage volume estimated during 1981–1990. (d) Damage volume estimated during 1990–2017. The damage values in panels (a), (c), and (d) are clipped at 5×10^{-5} and values below 5×10^{-6} are transparent.

quakes. Profile 2–2' along the SCTR has significant damage around Cajon Pass and San Gorgonio Pass. The profiles along various fault zones in Fig. 4 show concentration of background seismic activity and damage around 10–15 km depth. The results along the different profiles also show that the seismically active crust becomes shallower to the NE from the peninsular ranges to the Mojave, north of the SCTR, and to the SE along the SJF and Elsinore fault.

This last observation is confirmed by a region-wide analysis of the average depth of background events with magnitude $2 \leq M < 4$ (Fig. 5). The map shows the average depth of the examined events calculated with the same procedure and parameters as for the damage volume map in Fig. 2 (the only differences is that each grid point is assigned the average depth value, with no time averaging). The depth of the background seismicity in the analyzed

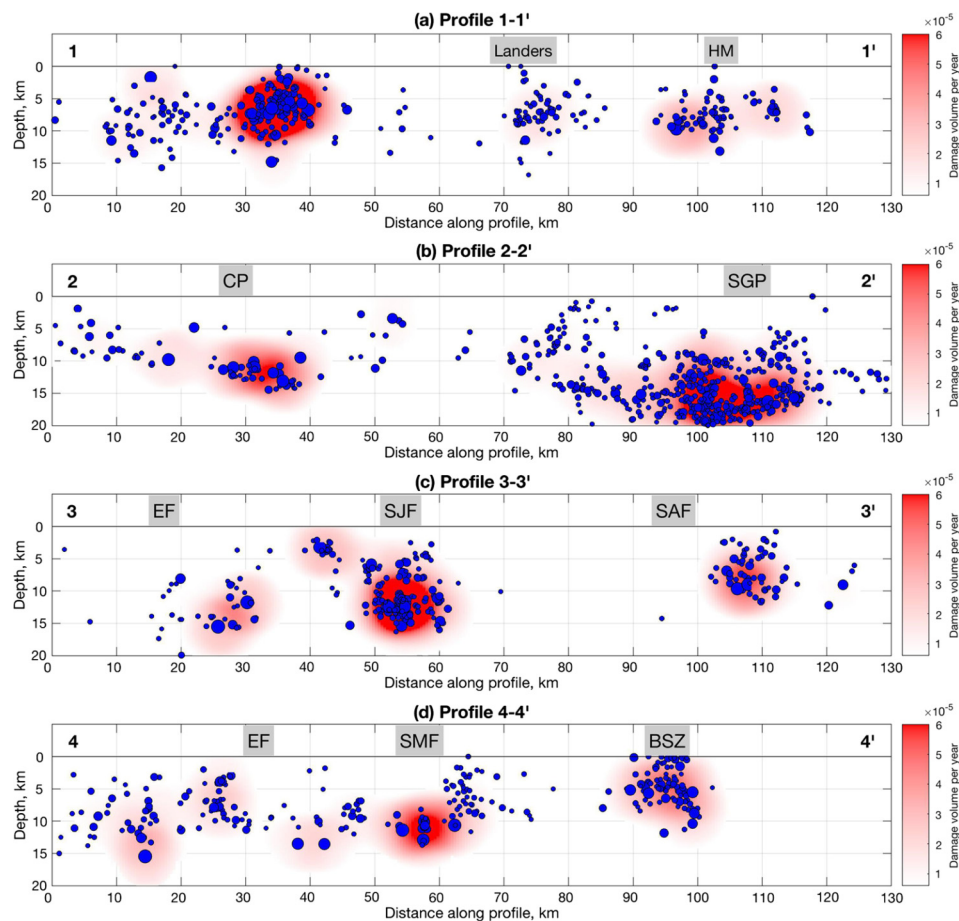


Fig. 3. Damage volume V in $\text{km}^3 \text{yr}^{-1}$ estimated along the numbered profiles shown in Fig. 1. Each profile plot is calculated using a rectangle with horizontal side coinciding with the profile on Fig. 1 and vertical extent of 20 km. The top part of each panel indicates the profile index and intersection with major seismogenic structures: Landers rupture area, M7.3, 1992; Hector Mine rupture area (HM), M7.1, 1999; Cajon Pass (CP); San Gorgonio Pass (SGP); Elsinore Fault (EF); San Jacinto Fault (SJF); San Andreas Fault (SAF); Superstition Mountain Fault (SMF); and Brawley Seismic Zone (BSZ). The damage values are clipped at 5×10^{-5} and values below 5×10^{-6} are transparent.

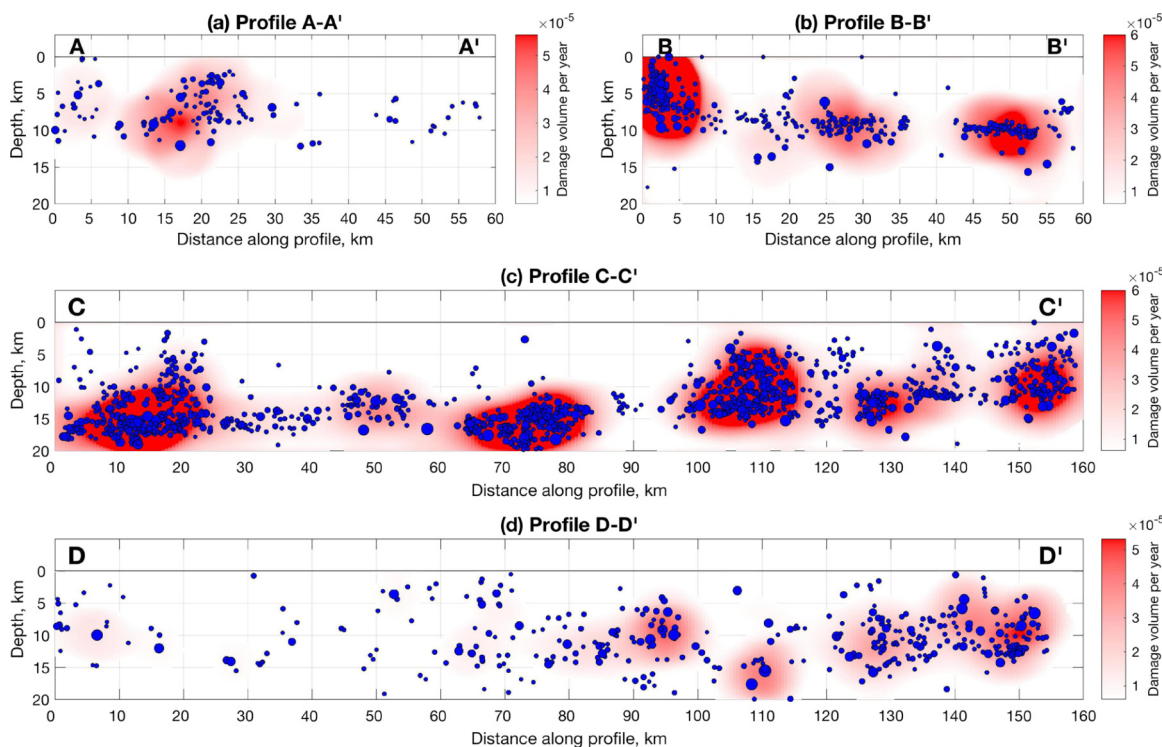


Fig. 4. Similar to Fig. 3 for damage volume V in $\text{km}^3 \text{yr}^{-1}$ estimated along the (along-fault) lettered profiles shown in Fig. 1.

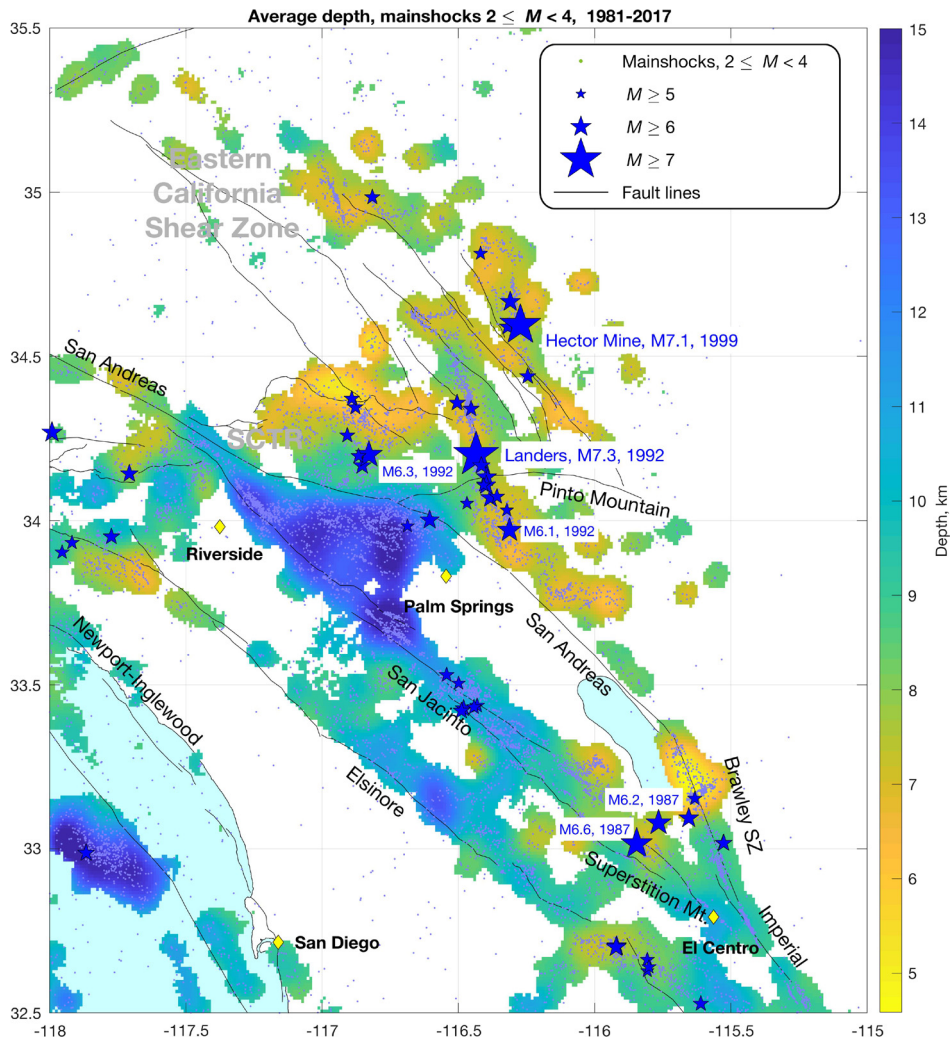


Fig. 5. Average depth in km (color code) of background events with magnitude $2 \leq M < 4$ during 1981–2017 used in this study for damage estimation. The depth map is clipped at 15 km. The other notations are as in Fig. 1.

magnitude range steadily decreases in the NE direction across the examined region, from about 10 km off-shore and along the Elsinore fault to about 5 km along and NE of the San Andreas Fault. In addition, there are two regions of deep background seismicity, between the SAF and SJFZ southeast of Cajon Pass and an offshore region in the southwest, with average depth of the examined seismicity beyond 15 km where the map is clipped. We also note the abrupt gradient in the depth of the background seismicity across the SCTR section of the SAF. To examine further the depth dependence of damage production we show in Fig. 6 the average yearly rock damage production by events with depth shallower (panel a) and deeper (panel b) than 7.5 km. The results show clearly that the rock damage production is far more continuous and intense below 7.5 km than it is in the shallower crust.

4. Discussion

We use basic theoretical relations for rupture area and volume (Eqs. (7) and (12)) generated by a population of earthquakes that satisfy the Gutenberg-Richter frequency-magnitude relation (1) to estimate the spatial variations of rock damage in southern California. The analysis employs the earthquake catalog of Hauksson et al. (2012) extended for the period 1981–2017. To obtain temporally stable results representing typical activity during an inter-seismic period on all faults, we use events in a narrow magnitude range ($2 \leq M < 4$) from a declustered version of the catalog. The results

highlight regions that sustain ongoing occurrence of background earthquakes, and provide reference values that can help interpreting models of seismic velocities and attenuation coefficients in the region. The estimated prominent damage zones represent the seismically active configuration of the plate-boundary in southern California, rather than reflecting transient activity associated with moderate-large events that happened to occur in the region during the last 37 yr.

The analysis assumes temporal statistical stability of the parameters in Eqs. (7) and (12). These include the Gutenberg-Richter a and b values; parameters k , e that connect earthquake potency and magnitude; rupture parameters γ , $\Delta\varepsilon$; and a magnitude range $M_1 \leq M \leq M_2$. Analyses of various data sets suggest that parameters b , k , e , γ , and $\Delta\varepsilon$ are relatively constant in time (Ben-Zion, 2008, and references therein). Temporal variations of these parameters are an order of magnitude smaller than changes of seismic intensity associated with the parameter a , produced by the irregular occurrence of medium-to-large events along with aftershock sequences and swarms. To alleviate these principal sources of time variations, we use only background events in the magnitude range $2 \leq M < 4$ from a declustered catalog based on the approach of Zaliapin and Ben-Zion (2013, 2016). This ensures that the a -values throughout the region are stable within the examined time interval. We argue that the apparent fluctuations of a -values, evident in analysis of the instrumental catalog, are associated with

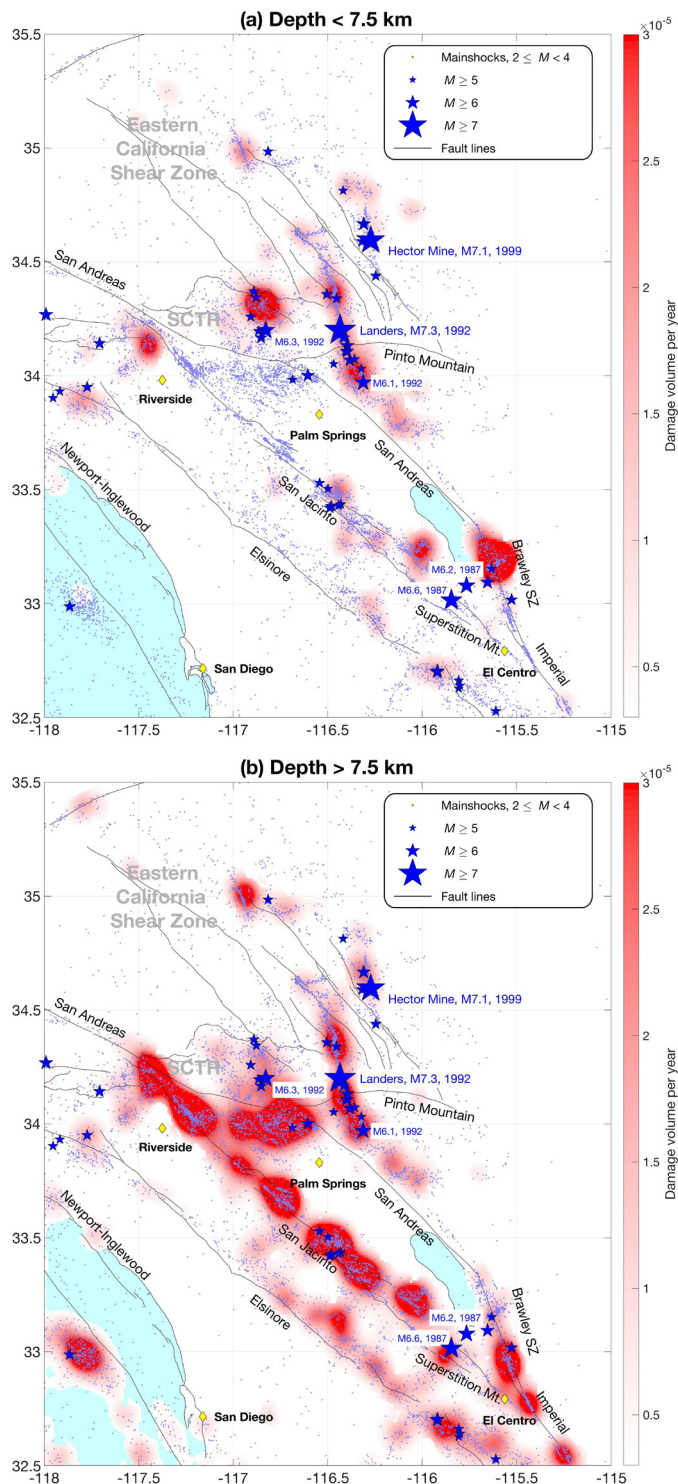


Fig. 6. Estimated damage volume V in $\text{km}^3 \text{yr}^{-1}$ for depth sections above 7.5 km (a) and below 7.5 km (b). The damage values are clipped at 3×10^{-5} and values below 3×10^{-6} are transparent. The other notations are as in Fig. 1.

moderate-large events and their aftershock sequences, and do not reflect changes of average inter-seismic a -values. These are likely to evolve only slowly, on a geological timescale, in conjunction with the slow evolution of the governing deformation regime. The results in Fig. 2b-d confirm the overall temporal stability of the obtained estimations and support the validity of our approach and assumptions. The presented results are unavoidably affected to some extent by temporal variations of seismic activity that we

cannot overcome with the available data. The temporal stability can be further improved by decreasing the lower magnitude M_1 , which could be possible in catalogs with lower completeness magnitude.

The features with prominent rocks damage in Fig. 2a are correlated well with low velocity zones in detailed tomographic results in the area (e.g. Shaw et al., 2015; Fang et al., 2016; Share et al., 2019). The largest continuous region of ongoing inter-seismic damage production is associated with the San Jacinto fault zone (Fig. 2a). The Elsinore fault forms a continuous structure of ongoing activity that is less pronounced than the SJFZ. We also observe several damage zones that are normal to (and extend between) the Elsinore and SJFZ, and may be associated with margins of active basins between the two faults (e.g., Axen and Fletcher, 1998). The rock damage maps in Fig. 2 point to the possible existence of a large-scale active seismic zone that connects the Imperial fault and Brawley seismic zone in the south with the ECSZ to the north. This is consistent with suggestions based on geodetic data and models that the southern SAF is in the process of being replaced by such a zone (e.g., Dokka and Travis, 1990; Nur et al., 1993; Thatcher et al., 2016).

A broad active damage zone exists around the San Andreas fault in the SCTR, and is especially pronounced around Cajon Pass, San Gorgonio Pass, the region around the 1992 M6.3 Big Bear earthquake, and generally south of the SAF. The results along profile 2–2' (Fig. 3b) further illustrate the broad damage zone under Cajon Pass and even more so below San Gorgonio Pass. Receiver function analyses show that the Moho geometry has significant changes below the SCTR (Zhu and Kanamori, 2000; Ozakin and Ben-Zion, 2015). Numerical simulations of evolving fault structures in a damage rheology model indicate that significant perturbations in the Moho geometry tend to suppress fault localization in the overlying crust and produce broad region of brittle deformation (Lyakhovsky and Ben-Zion, 2009). This is consistent with the observed broad damage zone in the SCTR.

Importantly, the rupture zones of the 1992 M6.1 Joshua Tree, M7.3 Landers and M6.3 Big Bear earthquakes have ongoing background seismicity and damage production before 1990 that outline the areas of future events (Fig. 2c). The 1999 M7.1 Hector Mine event was also preceded by increased damage production in its vicinity that started after the Landers earthquake (this is not shown in the presented results but indicated by calculating maps as in Fig. 2 during 1992–1999). We also notice that several clusters of $M > 5$ events occur in regions with high damage production by the ongoing background events. These results suggest that moderate and large events are preceded by a weakening damage process in volumes around the rupture zones of the eventual events. We note that this type of regional preparation process is fundamentally different than small-scale processes like sub-critical crack growth or small expanding nucleation zones on frictional surfaces leading to local instabilities (e.g., Rice, 1993; Ohnaka, 2003; Ben-Zion, 2008). The latter are relevant for initiation of ruptures, while the former is relevant for the size of the generated events.

Several plots of rock damage along vertical profiles that are parallel and normal to the major faults in the region (Figs. 3, 4) show that the seismogenic crust becomes shallower to the NE (profiles 3, 4) from the peninsular ranges to the Mojave, north of the SCTR, and to the SE along the SJFZ and Elsinore fault (profiles B, C). The profiles display prominent concentrations of rock damage across large faults and rupture zones, especially near major fault junctions, and show that the background seismic activity and rock damage in southern California are concentrated in the depth range of 10–15 km. The average depth of the background seismicity (Fig. 5) illustrates clearly the decreasing width of the seismically active crust in southern California to the NE, as well as

to the SE near the US–Mexico border, along with abrupt change in the average seismicity depth across the SAF in the SCTR consistent with depth variations of the Moho in the area. The vertical profile results also show that the background seismicity and rock damage production are concentrated in the depth range 10–15 km. This is demonstrated in Fig. 6, where the damage zones are shown to be quite patchy in the top 7.5 km and more pronounced and continuous along-strike of main faults in the deeper crust. These results are consistent with increasing seismic energy release and increasing localization of fault structures with depth.

The ongoing damage generation around the rupture zones of the Joshua Tree, Landers, Big Bear and Hector Mine earthquakes before the occurrence of these events, and location of most $M > 5$ events within pronounced damage zones, motivate additional analyses of spatio-temporal variations of rock damage in time intervals leading to moderate and large events. This will be done in a follow up work.

Acknowledgements

The study employs the southern California earthquake catalog of Hauksson et al. (2012; extended to later years). The research was supported by the National Science Foundation (grants EAR-1723033 and EAR-1722561), the Earthquake Hazards Program of the USGS (grants G17AP00086 and G17AP00087) and the Southern California Earthquake Center (based on NSF Cooperative Agreement EAR-1600087 and USGS Cooperative Agreement G17AC00047). The paper benefited from useful comments by two anonymous referees.

References

- Allam, A.A., Ben-Zion, Y., Kurzon, I., Vernon, F.L., 2014. Seismic velocity structure in the Hot Springs and Trifurcation areas of the San Jacinto fault zone, California, from double-difference tomography. *Geophys. J. Int.* 198, 978–999. <https://doi.org/10.1093/gji/ggu176>.
- Atkinson, G.M., Eaton, D., Ghofrani, H., Walker, D., Cheadle, B., Schultz, R., Shcherbakov, R., Tiampo, K., Gu, J., Harrington, R.M., Liu, Y., van der Baan, M., Kao, H., 2016. Hydraulic fracturing and seismicity in the Western Canada Sedimentary Basin. *Seismol. Res. Lett.* 87, 631–647.
- Axen, G.J., Fletcher, J.M., 1998. Late Miocene–Pleistocene extensional faulting, northern Gulf of California, Mexico and Salton Trough, California. *Int. Geol. Rev.* 40 (3), 217–244.
- Ben-Zion, Y., 2008. Collective behavior of earthquakes and faults: continuum-discrete transitions, evolutionary changes and corresponding dynamic regimes. *Rev. Geophys.* 46, RG4006. <https://doi.org/10.1029/2008RG000260>.
- Ben-Zion, Y., Ampuero, J.-P., 2009. Seismic radiation from regions sustaining material damage. *Geophys. J. Int.* 178, 1351–1356. <https://doi.org/10.1111/j.1365-246X.2009.04285.x>.
- Ben-Zion, Y., Zhu, L., 2002. Potency-magnitude scaling relations for southern California earthquakes with $1.0 < ML < 7.0$. *Geophys. J. Int.* 148, F1–F5.
- Dokka, R.K., Travis, C.J., 1990. Role of the eastern California shear zone in accommodating Pacific-North American plate motion. *Geophys. Res. Lett.* 17 (9), 1323–1326.
- Dresen, G., Gueguen, Y., 2004. Damage and rock physical properties. In: Guéguen, Y., Boutea, M. (Eds.), Mechanics of Fluid Saturated Rocks. In: International Geophysics Series. Elsevier, pp. 169–217.
- Eberhart-Phillips, D., Thurber, C., Fletcher, J.B., 2014. Imaging P and S attenuation in the Sacramento–San Joaquin delta region, Northern California. *Bull. Seismol. Soc. Am.* 104, 2322–2336.
- Edwards, B., Allmann, B., Fah, D., Clinton, J., 2010. Automatic computation of moment magnitudes for small earthquakes and the scaling of local to moment magnitude. *Geophys. J. Int.* 183, 407–420.
- Eshelby, J.D., 1957. The determination of the elastic field of an ellipsoidal inclusion and related problems. *Proc. R. Soc. Lond. Ser. A* 241, 376–396.
- Fang, H., Zhang, H., Yao, H., Allam, A., Zigone, D., Ben-Zion, Y., Thurber, C., van der Hilst, R.D., 2016. A new three-dimensional joint inversion algorithm of body-wave and surface-wave data and its application to the Southern California Plate Boundary Region. *J. Geophys. Res.* 121, 3557–3569. <https://doi.org/10.1002/2015JB012702>.
- Hamiel, Y., Liu, Y., Lyakhovsky, V., Ben-Zion, Y., Lockner, D., 2004. A visco-elastic damage model with applications to stable and unstable fracturing. *Geophys. J. Int.* 159, 1155–1165. <https://doi.org/10.1111/j.1365-246X.2004.02452.x>.
- Hanks, T.C., Kanamori, H., 1979. A moment magnitude scale. *J. Geophys. Res.* 84 (B5), 2348–2350.
- Hauksson, E., Shearer, P.M., 2006. Attenuation models (QP and QS) in three dimensions of the southern California crust: inferred fluid saturation at seismogenic depths. *J. Geophys. Res.* 111, B05302.
- Hauksson, E., Yang, W., Shearer, P.M., 2012. Waveform relocated earthquake catalog for southern California (1981 to June 2011). *Bull. Seismol. Soc. Am.* 102 (5), 2239–2244.
- Hickman, S., Sibson, R., Bruhn, R., 1995. Introduction to special section: mechanical involvement of fluids in faulting. *J. Geophys. Res.* 100, 12831–12840.
- Jamtveit, B., Ben-Zion, Y., Renard, F., Austrheim, H., 2018. Earthquake-induced transformation of the lower crust. *Nature* 556, 487–491. <https://doi.org/10.1038/s41586-018-0045-y>.
- Lin, G., Shearer, P.M., Hauksson, E., Thurber, C.H., 2007. A three-dimensional crustal seismic velocity model for southern California from a composite event method. *J. Geophys. Res.* 112, B11306. <https://doi.org/10.1029/2007JB004977>.
- Lockner, D., Walsh, J., Byerlee, J., 1977. Changes in seismic velocity and attenuation during deformation of granite. *J. Geophys. Res.* 82, 5374–5378.
- Lyakhovsky, V., Ben-Zion, Y., 2009. Evolving geometrical and material properties of fault zones in a damage rheology model. *Geochem. Geophys. Geosyst.* 10, Q11011. <https://doi.org/10.1029/2009GC002543>.
- Lyakhovsky, V., Ben-Zion, Y., Agnon, A., 2001. Earthquake cycle, fault zones, and seismicity patterns in a rheologically layered lithosphere. *J. Geophys. Res.* 106, 4103–4120.
- Marc, O., Hovius, N., Meunier, P., Uchida, T., Hayashi, S., 2015. Transient changes of landslide rates after earthquakes. *Geology* 43, 883–886. <https://doi.org/10.1130/G36961.1>.
- Mavko, G., Mukerji, T., Dvorkin, J., 2009. The Rock Physics Handbook: Tools for Seismic Analysis of Porous Media. Cambridge University Press.
- Nur, A., Ron, H., Beroza, G.C., 1993. The nature of the Landers–Mojave earthquake line. *Science* 261, 201–203.
- Ohnaka, M., 2003. A constitutive scaling law and a unified comprehension for frictional slip failure, shear fracture of intact rock, and earthquake rupture. *J. Geophys. Res.* 108 (B2), 2080. <https://doi.org/10.1029/2000JB000123>.
- Ozakin, Y., Ben-Zion, Y., 2015. Systematic receiver function analysis of the Moho geometry in the Southern California plate-boundary region. *Pure Appl. Geophys.* 172, 1167–1184. <https://doi.org/10.1007/s00024-014-0924-6>.
- Peng, S., Johnson, A.M., 1972. Crack growth and faulting in cylindrical specimens of Chelmsford granite. *Int. J. Rock Mech. Min. Sci.* 9, 37–86.
- Renard, F., Weiss, J., Mathiesen, J., Ben Zion, Y., Kandula, N., Cordonnier, B., 2018. Critical evolution of damage towards system-size failure in crystalline rock. *J. Geophys. Res.* 123, 1969–1986. <https://doi.org/10.1002/2017JB014964>.
- Rice, J.R., 1993. Spatio-temporal complexity of slip on a fault. *J. Geophys. Res.* 98, 9885–9907.
- Ross, Z.E., Ben-Zion, Y., White, M.C., Vernon, F.L., 2016. Analysis of earthquake body wave spectra for potency and magnitude values: implications for magnitude scaling relations. *Geophys. J. Int.* 207, 1158–1164. <https://doi.org/10.1093/gji/ggw327>.
- Scheingross, J.S., Minchew, B.M., Mackey, B.H., Simons, M., Lamb, M.P., Hensley, S., 2013. Fault zone controls on the spatial distribution of slow moving landslides. *Geol. Soc. Am. Bull.* 125, 473–489. <https://doi.org/10.1130/B30719.1>.
- Schoenball, M., Ellsworth, W.L., 2017. A systematic assessment of the spatio-temporal evolution of fault activation through induced seismicity in Oklahoma and southern Kansas. *J. Geophys. Res., Solid Earth* 122, 10,189–10,206. <https://doi.org/10.1002/2017JB014850>.
- Share, P.-E., Guo, H., Thurber, C.H., Zhang, H., Ben-Zion, Y., 2019. Seismic imaging of the southern California plate-boundary around the South-Central Transverse Ranges using double-difference tomography. *Pure Appl. Geophys.* 176. <https://doi.org/10.1007/s00024-018-2042-3>.
- Shaw, J.H., Plesch, A., Tape, C., Suess, M.P., Jordan, T.H., Ely, G., Hauksson, E., Tromp, J., Tanimoto, T., Graves, R., Olsen, K., Nicholson, C., Maechling, P.J., Rivero, C., Lovely, P., Brankman, C.M., Munster, J., 2015. Unified structural representation of the southern California crust and upper mantle. *Earth Planet. Sci. Lett.* 415, 1–15.
- Sibson, R.H., 2011. The scope of earthquake geology. In: Fagereng, A., Toy, V., Rowland, J. (Eds.), Geology of the Earthquake Source: A Volume in Honour of Rick Sibson. In: Geological Society of London Special Publication, vol. 359, pp. 319–331.
- Sibson, R.H., Moore, J.M., Rankin, A.H., 1975. Seismic pumping: a hydrothermal fluid transport mechanism. *J. Geol. Soc. Lond.* 131, 653–659.
- Thatcher, W., Savage, J.C., Simpson, R.W., 2016. The Eastern California Shear Zone as the northward extension of the southern San Andreas Fault. *J. Geophys. Res., Solid Earth* 121. <https://doi.org/10.1002/2015JB012678>.
- Wechsler, N., Rockwell, T.K., Ben-Zion, Y., 2009. Application of high resolution DEM data to detect rock damage from geomorphic signals along the central San Jacinto Fault. *Geomorphology* 113, 82–96. <https://doi.org/10.1016/j.geomorph.2009.06.007>.
- Zaliapin, I., Ben-Zion, Y., 2013. Earthquake clusters in southern California I: identification and stability. *J. Geophys. Res.* 118, 2847–2864. <https://doi.org/10.1002/jgrb.50179>.

- Zaliapin, I., Ben-Zion, Y., 2016. A global classification and characterization of earthquake clusters. *Geophys. J. Int.* 207, 608–634. <https://doi.org/10.1093/gji/ggw300>.
- Zhu, L., Kanamori, H., 2000. Moho depth variation in southern California from teleseismic receiver functions. *J. Geophys. Res., Solid Earth (1978–2012)* 105 (B2), 2969–2980.